Accurate drift-invariant single-molecule force calibration using the Hadamard variance

Stefanie D. Pritzl, Alptuğ Ulugöl, Caroline Körösy, Laura Filion, Jan Lipfert

Angaben zur Veröffentlichung / Publication details:

Pritzl, Stefanie D., Alptuğ Ulugöl, Caroline Körösy, Laura Filion, and Jan Lipfert. 2024. "Accurate drift-invariant single-molecule force calibration using the Hadamard variance." *Biophysical Journal* 123 (22): 3964–76. https://doi.org/10.1016/j.bpj.2024.10.008.

Biophysical Journal
Article

Biophysical Society

Accurate drift-invariant single-molecule force calibration using the Hadamard variance

Stefanie D. Pritzl,[1,*] Alptuğ Ulugöl,[1] Caroline Körösy,[1] Laura Filion,[1,*] and Jan Lipfert[1,2,*]
[1]Soft Condensed Matter and Biophysics, Department of Physics and Debye Institute for Nanomaterials Science, Utrecht University, Utrecht, the Netherlands and [2]Institute for Physics, Augsburg University, Universitätsstrasse 1, Augsburg, Germany

ABSTRACT Single-molecule force spectroscopy (SMFS) techniques play a pivotal role in unraveling the mechanics and conformational transitions of biological macromolecules under external forces. Among these techniques, multiplexed magnetic tweezers (MT) are particularly well suited to probe very small forces, ≤ 1 pN, critical for studying noncovalent interactions and regulatory conformational changes at the single-molecule level. However, to apply and measure such small forces, a reliable and accurate force-calibration procedure is crucial. Here, we introduce a new approach to calibrate MT based on thermal motion using the Hadamard variance (HV). To test our method, we perform bead-tether Brownian dynamics simulations that mimic our experimental system and compare the performance of the HV method against two established techniques: power spectral density (PSD) and Allan variance (AV) analyses. Our analysis includes an assessment of each method's ability to mitigate common sources of additive noise, such as white and pink noise, as well as drift, which often complicate experimental data analysis. We find that the HV method exhibits overall similar or higher precision and accuracy, yielding lower force estimation errors across a wide range of signal-to-noise ratios (SNRs) and drift speeds compared with the PSD and AV methods. Notably, the HV method remains robust against drift, maintaining consistent uncertainty levels across the entire studied SNR and drift speed spectrum. We also explore the HV method using experimental MT data, where we find overall smaller force estimation errors compared with PSD and AV approaches. Overall, the HV method offers a robust method for achieving sub-pN resolution and precision in multiplexed MT measurements. Its potential extends to other SMFS techniques, presenting exciting opportunities for advancing our understanding of mechanosensitivity and force generation in biological systems. To make our methods widely accessible to the research community, we provide a well-documented Python implementation of the HV method as an extension to the Tweezepy package.

SIGNIFICANCE Single-molecule force spectroscopy techniques are vital for studying the mechanics and conformations of biomacromolecules under external forces. Multiplexed magnetic tweezers (MT) excel in applying forces ≤ 1 pN, which are critical for examining noncovalent interactions and regulatory changes at the single-molecule level. Precise and reliable force calibration is essential for these measurements. In this study, we present a new force-calibration method for MT using Hadamard variance (HV) to analyze the thermal motion of DNA-tethered beads. The HV method shows similar or higher precision and accuracy to established techniques such as power spectral density and Allan variance. Most significantly, it is drift-invariant, maintaining consistent performance across varying experimental conditions. This robustness against drift ensures reliable force application and measurements at sub-pN resolution.

INTRODUCTION

Single-molecule force spectroscopy (SMFS) techniques have emerged as powerful tools to investigate the behavior of biological macromolecules under forces and torques (1–6). SMFS measurements have provided comprehensive insights into various biological processes, such as, e.g., the function of molecular motors and DNA and protein mechanics (6–12), interaction potentials between receptor-ligand pairs or DNA and different binding agents (13–15), as well as protein folding pathways and associated dynamics (16–18). For many biologically relevant questions, it is critical to resolve low forces in the sub-pN range (≤ 1 pN), e.g., to reveal specific protein interactions or small conformational changes involved in regulatory processes including cell motility, development, and differentiation. Here, MT offer several important advantages compared with other

Submitted June 17, 2024, and accepted for publication October 10, 2024.
*Correspondence: s.d.pritzl@uu.nl or l.c.filion@uu.nl or j.lipfert@uu.nl
Stefanie D. Pritzl and Alptuğ Ulugöl contributed equally to this work.
Editor: Jonathon Howard.
https://doi.org/10.1016/j.bpj.2024.10.008

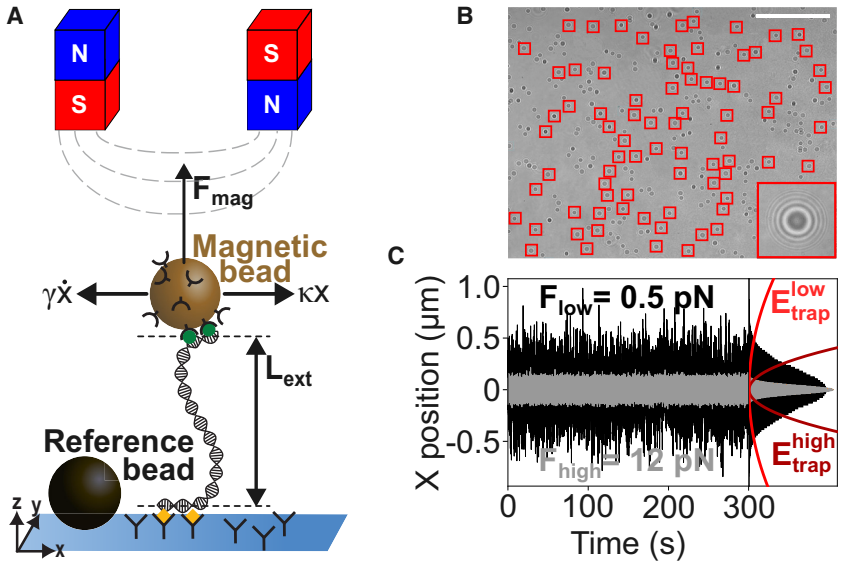

FIGURE 1 Schematic of a magnetic tweezers setup. (*A*) The DNA with an extension L_{ext} is tethered between a substrate and a superparamagnetic bead. External magnets exert a magnetic force (F_{mag}) on the bead. Drag γ and trap stiffness κ act on the bead parallel and vertical to the substrate in all three dimensions x, y, and z (for simplicity, only highlighted in the x direction). (*B*) Field of view of our MT setup. Red squares highlight 78 beads that were tracked over time. The inset shows a zoom of one bead's diffraction ring pattern used for tracking. Scale bar, 100 μm. (*C*) Example (simulated) time traces of transverse fluctuations for different magnetic forces (*left*) and trap energy landscapes (*right*). The histograms on the right are computed from the time traces on the left.

established SMFS techniques such as optical tweezers and atomic force microscopy (5,19–21): MT provide access to a large force range of $\sim 0.01 - 100$ pN with high stability and accuracy and high resolution in particular at low forces and in a multiplexed format to measure hundreds of molecules at the same time (1,6,12,22–26). The latter is essential to obtain sufficient statistics from a single experiment, to observe rare events and identify molecular subpopulations, and to test diverse conditions and stimuli. Furthermore, MT intrinsically measure at constant force without the need for feedback control (12) and do not suffer from heat generation or photodamage (27), which permits stable measurements on timescales ranging from submilliseconds to weeks (22,28). Notably, various magnet geometries have been used to not only apply constant forces, but also to control and monitor torque and twist at the molecular level (29–31).

In MT, molecules of interest are tethered between a functionalized surface and small superparamagnetic beads (Fig. 1 *A*). External magnets exert controlled forces and torques on the beads and subsequently to the molecule of interest. To achieve highly parallel or multiplexed measurements, cameras with tens of megapixels can be used to image large fields of view (≥ 0.5 mm^2). Hence, tracking of tens to hundreds of tethered beads at the same time becomes possible (Fig. 1 *B*), while applying constant forces across the field of view (22). A first key step in SMFS measurement is to perform an accurate force calibration to obtain exact and reproducible results. The most common approach for calibrating the forces is to make use of the bead's thermal motion (32–34). This method makes use of the equipartition theorem, which links the variance of thermal motion to the trap stiffness of the system and the thermal energy k_BT, where k_B is the Boltzmann constant and T the temperature. Since the temperature of the system is easy to measure, calibration using thermal motion tends to be more accurate and reliable than alternative methods based on, e.g., bead sedimentation dynamics (27,35,36) or calculations of the magnetic field and exerted force (37).

In the thermal motion-based force-calibration procedure, the bead is trapped in a harmonic potential originating from the combination of forces from the external magnetic field and from the elastic response of the molecular tether (34). One calibrates the forces by analyzing the thermal trajectory of the bead (32). Typically, long (> 1 μm in contour length) double-stranded DNA (dsDNA) molecules are used for this force-calibration method, due to their well-known properties and force-response characteristics. In particular, at low forces the force-extension relation for dsDNA is well described by the worm-like chain (WLC) model (38–40). In addition, DNA undergoes a sharp overstretching transition at ~ 65 pN resulting in a structural transition and corresponding abrupt length increase (41). Moreover, long dsDNA molecules make it relatively easy to accurately determine the thermal motion of the attached magnetic beads for several reasons (42–44). First, tracking errors (typically $1 - 2$ nm) matter less for long tethers (45–47). Second, long DNA tethers result in larger characteristic times and hence slower thermal bead motion, which reduces the impact of finite camera exposure times (34,42,48,49). Third, off-center attachment (50) of a long DNA strand to the magnetic bead is less of an issue than for short tethers, since the extension of the tether is much larger than the bead radius.

At long observation times ($\tau \gg 10^{-4}$ s), hydrodynamic effects between the bead and its aqueous environment can be neglected (51) and the bead motion is well described by the overdamped Langevin equation, which contains

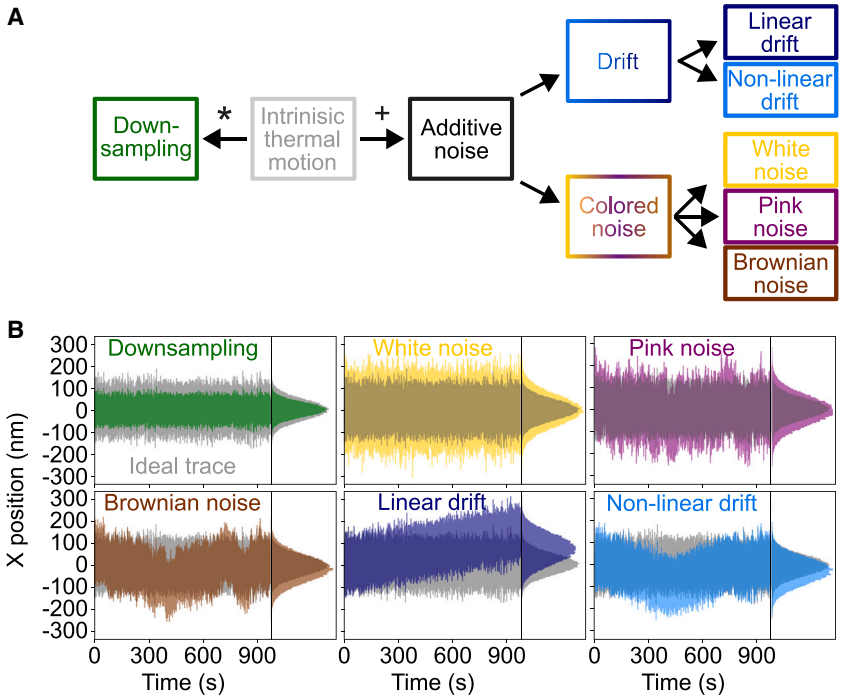

FIGURE 2 Overview of processes affecting time traces of tracked beads in MT. (*A*) Classification of the spatial and temporal alterations of the intrinsic thermal motion. Downsampling acts as a low-pass filter introducing blurring and aliasing and is denoted as "$*$", as it effectively acts as a convolution of the signal. Additive noise contributions denoted as "$+$". We differentiate between drift (linear and nonlinear) and colored noises (white, pink, and Brownian noise). (*B*) Example traces for downsampling and different additive noise types. The unaltered (ideal) thermal motion bead trace for a sampling frequency of 10 kHz is shown in gray in all panels; the same trace downsampled to 72 Hz is shown in green. White, pink, and Brownian noise, and linear and nonlinear drift contaminated traces for signal-to-noise ratios (SNRs) of $-$ 2.4, $-$ 1.6, 0.6, $-$ 9.7, and 0.9 dB, respectively, are shown in the colors indicated in the legend. All traces were obtained via Brownian dynamics simulations (materials and methods) assuming a force of 2.5 pN and a 1 μm bead. The individual SNRs were chosen for visualization purposes.

two parameters, the drag coefficient γ of the bead and the harmonic trap stiffness κ (42). Using the equipartition theorem, the trap stiffness κ, which in turn is related to the force, can be determined from the transverse thermal motion of the tethered magnetic bead (33,34). Specifically, for a magnetic bead confined to a harmonic trap in the MT, the equipartition theorem gives the real-space variance (RSV) by.

$$\sigma_i^2 = \frac{k_B T}{\kappa_i}, \tag{1}$$

where $i \in \{x,y,z\}$, k_B is the Boltzmann constant, and T is the temperature. Here, κ_i is the spring constant of the trap along the i^{th} direction. Hence, stiff and soft traps result in small and large variances of the bead trajectory, respectively (Fig. 1 *C*). Conversely, if we measure the bead displacement at a known temperature T, we can calculate the trap stiffness κ_i for each direction.

In particular, the variance of bead motion in the transverse direction parallel to the magnetic field is directly related to the applied force F_z via (34).

$$F_z = \kappa_{\parallel}\langle z\rangle = \frac{k_B T\langle z\rangle}{\sigma_{\parallel}^2}, \tag{2}$$

where $\langle z\rangle$ is the mean extension of the molecule in the z direction. Note that, in principle, we could make use of the fluctuations that are perpendicular to both the F_z and the magnetic field, but in that case the measured extension of the molecule must be corrected to include rotation of the bead in the magnetic field (42).

While conceptually straightforward, the RSV approach has two key limitations: first, due to the finite shutter time in camera-based tracking, the acquired signal is distorted due to motion blurring and temporal aliasing (termed downsampling throughout this work, Fig. 2 *A*), which act as a low-pass filter and lead to underestimation of the true variance (42,48,49). Hence, spatiotemporal information is lost if the sampling frequency is too low, which leads to an overestimation of the applied forces (Fig. 2 *B*). Errors due to the finite shutter time are particularly problematic for short tethers and high forces since the characteristic time of the intrinsic fluctuations decreases with increasing force and decreasing tether length. A number of approaches have been put forward to overcome the limitations due to finite shutter time, including high-frequency tracking (43,47), shuttered illumination (44,48), and the application of spectral corrections in the analysis (42).

The second key limitation of the RSV approach is that it is susceptible to any kind of additive noise (52), which affects MT measurements by introducing spatial alterations and bias to fitting algorithms (53) (Fig. 2 *B*). Note that we explicitly distinguish here between the intrinsic thermal Brownian bead motion (sometimes also referred to as "noise" in the literature), which is our "signal" in the context of force calibration, and additional detrimental spatial alterations, which we call "additive noises" (Fig. 2 *A*). Among the types of additive noises, colored noises, which follow a power-law spectrum, are well-known sources for spatial distortions. There are three common types of colored noise that can, in particular, cause

erroneous force calibration of SMFS systems (Fig. 2 *B*): first, the use of electric devices such as cameras in MT settings for data acquisition and computer-based signal processing generates white noise (54,55). White noise is an additive type of colored noise resulting in broadening of the bead trajectories and thereby underestimation of the force. Second, resistance fluctuations in the electronic components (camera, motors, etc.) (54) and structural relaxations of the DNA (56,57) (overstretching, solvent effects, etc.) can induce pink noise. Pink noise is also known as flicker noise and leads to random spatial shifts of the bead trajectory. Third, similar spatial shifts can also emerge from unaccounted physical processes (light-matter interactions, rotational bead motion, etc.) that generate Brownian noise (58) in addition to the thermal bead motion one wants to extract and analyze. Like white and pink noise, Brownian noise broadens the bead trajectories spatially and causes force underestimation.

To address the challenges associated with downsampling and colored noises, a number of extensions of Eq. 1 have been introduced to obtain a better estimation of $\kappa_{\parallel}$. These calibration methods include 1) the power spectral density (PSD) and iterative corrections of the camera effects (42), 2) the PSD with additional correction factors for tracking errors and colored noises (49), and 3) the Allan variance (AV) (49) method, which accounts for frequency instabilities. However, none of these calibration methods can handle drift, which is also a type of additive noise, and a well-known issue in SMFS experiments, in addition to downsampling and colored noises. While mechanical drift is commonly corrected for in MT by tracking reference beads (52), residual, uncorrected drift still remains in the data (46) and linear drift can occur over any time interval of the total measurement time (supporting material, section S1, Fig. S1). In particular in multiplexed MT with a large field of view, drift across the field of view can be an additional limiting issue (Fig. 2 *B*). The Hadamard variance (HV) (59) has been shown to offer significant advantages in handling drift in metrology contexts, as it uses a second-order finite difference method that renders it drift-invariant by definition by canceling linear contributions (60). Hence, in theory, the HV is more robust with respect to drift than the PSD and AV methods, and insensitive to linear drift. Furthermore, compared with the AV, the HV exhibits higher resolution in estimating the frequency spectrum since it has a smaller noise bandwidth (61).

To extend the existing force-calibration methods for multiplexed MT measurements, here we present a thermal motion-based model of the HV. We compare all three methods, i.e., PSD, AV, and HV, using simulated and experimental data traces. First, we test our method with simulated bead trajectories at forces ranging from 0.5 to 80 pN. We compare the thermal motion of an ideal trace to traces with various sources of error, including downsampling, white noise, pink noise, Brownian noise, and drift, at experimentally relevant signal-to-noise ratios (SNRs) and drift speeds. We simulate data with SNRs of -10 to $+30$ dB, which correspond to 10 times higher noise compared with signal levels and 1000 times higher signal compared with noise levels, respectively. Overall, we make two important observations: first, all three methods can account for colored noises, with the HV method being more precise at SNRs of ≤ 10 dB in the presence of Brownian noise. Second, the HV method is the most stable and accurate in the presence of linear and nonlinear drift over the whole studied SNR and drift speed ranges. Finally, application of the methods to experimental data and quantification of the goodness-of-fit show that the HV method gives the most precise force estimation values, as we find the relative force errors for the HV to be lower compared with PSD and AV. Overall, our findings highlight that the HV is a suitable tool to process multiplexed SMFS data sets to obtain accurate and precise results in the presence of colored noise and drift, which we expect to be useful for the calibration of force spectroscopy techniques and related applications.

MATERIALS AND METHODS

To determine the accuracy of the PSD, AV, and HV methods in handling downsampling, colored noise, and drift, we employ simulations, analytical theory, and experimental measurements. Here, we first describe our methodology to simulate the Brownian dynamics of the bead-tether system, including downsampling, colored noise, as well as linear and nonlinear drift. Second, we summarize the theoretical background and formulae for the PSD, AV, and HV methods, and third, the experimental details of the MT setup and force-calibration measurement are reported.

Notably, we focus on the Brownian motion along the axis parallel to the magnetic field, which we term x position throughout this work. In principle, all methods and procedures can also be applied to analyze the bead motion in the y direction perpendicular to the magnetic field. In this case, however, additional correction factors are needed that include free bead rotations (42). In the z direction, we are only interested in the mean extension ($L_{ext} = \langle z \rangle$) to calculate the magnetic force (Eq. 2). Although linear drift and other noises can lead to inaccuracies in the extension, the accuracy of the estimation of the trap stiffness is more critically affected, as it scales quadratically with measurement time compared with the linear scaling of the extension. In addition, the extension L_{ext} (e.g., ~ 7 μm in this work) is much larger than the linear drift contribution (< 0.05 μm/s), rendering the latter less significant.

Simulations of the bead-tether system and inclusion of downsampling, colored noise, and drift

Brownian dynamics simulations

Our goal is to mimic an experimental MT setting where a long dsDNA tether (21 kbp) is tethered between a bead and a surface. We model this as a bead-tether system in three dimensions. We assume that the bead is pulled by a constant magnetic force perpendicular to the hard wall and we model the DNA tether as a WLC whose contour (L_c) and persistence (L_p) lengths are 7 μm (corresponding to 21 kbp) and 45 nm, respectively (62). We note that we employ the inextensible WLC model, which does not include enthalpic stretching of DNA or the dsDNA overstretching transition around 65 pN (41), since the focus of our simulations is to highlight

the effects of various types of noise on the traces, not to build a more realistic model for DNA.

Furthermore, collisions between the magnetic bead and solvent molecules are included as a three-dimensional (3D) stochastic Langevin force F_L that depends on the proximity to the hard wall due to hydrodynamic effects. The 3D stochastic Langevin force F_L obeys the fluctuation-dissipation theorem $\langle F_L^{(i)}(t)F_L^{(j)}(t')\rangle = 2k_BT\gamma_{ij}(z)\delta(t-t')$ with $\delta(t-t')$ being the Dirac distribution and $\gamma_{ij}(z)$ the Faxén-corrected (62–64) diagonal viscous drag matrix elements that account for the hydrodynamics of the hard wall on the bead motion. By combining these effects, we arrive at the overdamped Langevin equation that describes the motion of the magnetic bead as

$$\gamma(z)\dot{\mathbf{r}}(t) - F_{mag}\hat{\mathbf{z}} + F_{WLC}\hat{\mathbf{r}} = \mathbf{F}_L(t), \tag{3}$$

with $r = (x, y, z)$ being the position vector ($\hat{\mathbf{r}} = \mathbf{r}/|\mathbf{r}|$), F_{mag} the magnitude of the magnetic force, and $F_{WLC}(r)$ the WLC force given by the 7-parameter WLC model (40). To numerically solve the equation of motion, we write Eq. 3 in the stochastic differential equation form,

$$\mathrm{d}r_i = a_i(\mathbf{r})\mathrm{d}t + \sum_{j=1}^{3} b_{ij}(z)\mathrm{d}W_j, \tag{4}$$

where $\boldsymbol{a}(\mathbf{r}) \equiv \gamma^{-1}(z)\left[F_{mag}\hat{\mathbf{z}} - F_{WLC}(r)\hat{\mathbf{r}}\right]$, $b_{ij}(z) \equiv \sqrt{2k_BT\gamma_{ij}^{-1}(z)}$, and W_j are independent Wiener processes. Then, we employ the Milstein method (65) to cast the stochastic differential equation into the recursive relation,

$$\begin{aligned} r_i(t+\Delta t) = {} & r_i(t) + a_i(\mathbf{r})\Delta t + \sum_{j=1}^{3} b_{ij}(z)\Delta W_j \\ & + \frac{1}{2}b_{33}(z)\frac{\partial b_{ii}(z)}{\partial z}\left(\Delta W_i \Delta W_3 - \Delta t\right), \end{aligned} \tag{5}$$

where $\Delta W_i \sim \mathcal{N}(0, \Delta t)$ is a Gaussian distributed random number with zero mean and variance Δt. The custom Python 3 code implementing our Brownian dynamics simulations of the bead-tether system is available at https://github.com/alptug/WLC-BD. Using the simulation method introduced above, we perform 50 independent simulations per magnetic force (0.5, 2.5, 12.0, 40.0, and 80.0 pN), microsphere size (representing the commonly used MyOne [diameter 1 μm] and M270 [diameter 2.8 μm] superparamagnetic beads), and SNRs (22, 500 simulations in total). We calculate the force estimates for each simulated trace and use the average force from the 50 independent simulations as the final force estimate. The error bars then correspond to the standard error.

Downsampling of simulation trajectories

We include downsampling as follows: we divide the simulation trajectory into nonoverlapping windows of width $1/f_s$ with f_s being the sampling frequency. Then, we calculate the average of each window, yielding samples separated by $1/f_s$ that form the desired downsampled trajectory. Temporal aliasing is intrinsically included as a consequence of the relation $h_{ds}(f) = \sum_{k=-\infty}^{\infty} h(|f + kf_{Nq}|)$ with $h(f)$ and $h_{ds}(f)$ being the Fourier transforms of the signal and downsampled signal, respectively.

Addition of colored noise and drift to simulation trajectories

To add colored noises, we follow a four-step recipe (66). 1) First, we generate independent sets of Gaussian random numbers whose length matches the trajectory length, which corresponds to white noise. 2) Then, we take the Fourier transform of the noise and rescale the frequency contributions to match the PSD profile of the colored noise, followed by taking an inverse Fourier transform to revert to real space. 3) Next, we calculate the powers of the pure signal and the noise by numerically integrating their autocorrelation function. We then rescale the noise to SNRs ranging from -10 to $+30$ dB, which covers and exceeds the range of noise typically encountered experimentally. Experimental SNRs are highly system specific and depend on factors such as the imaging technique, measurement duration, camera resolution, setup and tracking stability, and also day-to-day variations (46,47,67–69). To give a guideline for an upper bound of the SNR range, we estimate the noise profiles of the reference beads as described in the supporting material (section S5) and add it to an ideal trace. This procedure yields an SNR upper limit of $5 - 15$ dB. However, we emphasize that this range is specific for our MT system and will deviate for other instruments. 4) Finally, we add the rescaled noise to the ideal signal to obtain the noisy trace with a defined noise type and magnitude. To add linear drift to the trajectory, we add a line with defined slope, i.e., drift speeds of $0 - 50$ nm s^{-1}. To add nonlinear drift, we add colored noise with a PSD that is strongly peaked at low frequencies ($S(f) \propto 1/f^4$), using the same procedure as for the other colored noises.

Closed-form expressions for the PSD, AV, and HV

To use the PSD, AV, or HV to determine κ, we require expressions that relate measurements of these quantities to κ. To this end, we consider a simple model of the bead-tether system in one dimension. Specifically, we model the whole bead-tether system as a harmonic trap of stiffness κ centered at the equilibrium position. Collisions between bead and solvent molecules are modeled by a stochastic Langevin force F_L that obeys the fluctuation-dissipation relation given as $\langle F_L(t)F_L(t')\rangle = 2k_BT\gamma\delta(t-t')$, with γ being the viscous drag coefficient. The bead's motion is then well described by the overdamped Langevin equation

$$\kappa x(t) + \gamma\dot{x}(t) = F_L(t). \tag{6}$$

One way to infer the trap stiffness κ is the use of the RSV method, as described in the introduction. However, to also account for downsampling and colored noise types, including white, pink, and Brownian noise, closed-form expressions of the PSD and AV have been derived for the overdamped Langevin equation (Eq. 6) to extract the trap stiffness κ (see below). While the PSD and AV approaches have been used widely to obtain force estimates from tweezer time traces, they can be susceptible to drift and other measurement imperfections. Therefore, we derive here a closed-form expression of the HV for Eq. 6 to establish an accurate drift-invariant force-calibration technique. For clarity, we also visualize the impact of downsampling, colored noises, and linear and nonlinear drift on the PSD, AV, and HV methods (supporting material, section S2, Figs. S2 and S3).

Power spectral density

The PSD is a measure of the power contribution of the different signal frequency components to the total signal given as

$$S(f) = \int_{-\infty}^{\infty}\left(\int_{-\infty}^{\infty} x(t-\tau)x(t)\mathrm{d}t\right)e^{-2\pi f\tau}\mathrm{d}\tau. \tag{7}$$

The PSD $S(f)$ of the bead trajectory then follows from Fourier analysis of the overdamped Langevin equation (Eq. 6). The downsampling-corrected analytical closed-form expression of the PSD is given by (49,70).

$$S(f) = \frac{2k_BT\gamma}{\kappa^3}\left(\kappa + \frac{2\gamma f_s \sin^2\left(\frac{\pi f}{f_s}\right)\sinh\left(\frac{\kappa}{\gamma f_s}\right)}{\cos\left(\frac{2\pi f}{f_s}\right) - \cosh\left(\frac{\kappa}{\gamma f_s}\right)}\right), \tag{8}$$

with f_s the sampling frequency. Notably, Eq. 8 holds for the special case of equal finite camera exposure time τ_0 and sampling time $\tau_s = 1/f_s$, i.e., $\tau_0 = \tau_s$ (70). This assumption is applicable to most modern video cameras because the camera dead time ($\sim 10^{-6}$ s) is in general much smaller than the sampling time ($\sim 10^{-4}$ to 10^{-1} s). The PSD has a Lorentzian-like form with a turning point at the corner frequency (Fig. 3 *A*).

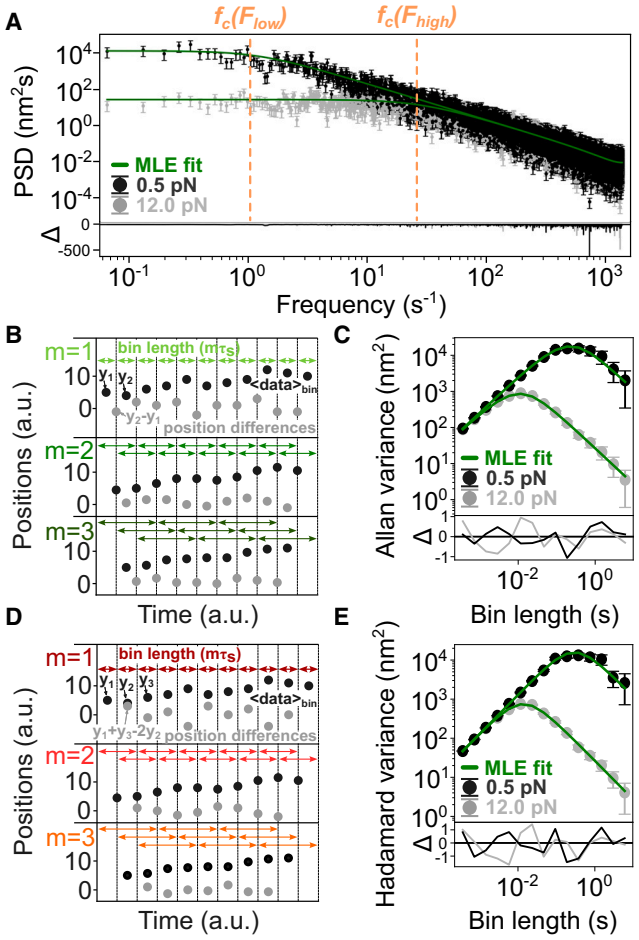

FIGURE 3 Illustration of the PSD, AV, and HV analyses. Example plots of the PSD (*A*), Allan variance (*C*), and Hadamard variance (*E*) methods applied to ideal, simulated bead trajectories. The lower parts (Δ) represent the residuals of the MLE fit to the simulated data. (*B* and *D*) Schematics of the position difference calculations for the Allan (*B*) and Hadamard (*D*) variance. The black dots for $m = 1$ are the original signal. The black dots for $m = 2$ and 3 are the position signals averaged over a bin comprising m points. The (first- and second-order) position differences are shown as gray dots and are derived from two and three consecutive data points for Allan and Hadamard variance, respectively. The arrows in panels *B* and *D* represent the bin lengths; error bars in panels *A*, *C*, and *E* correspond to one standard error.

Allan variance

The AV of the bead's thermal motion is computed by separating the signal into different observation time intervals or bins of length τ, and calculating the first position differences (first-order finite difference method), i.e., the differences of two consecutive averaged data points, as a function of the observation time bins (Fig. 3, *B* and *C*). Specifically, we calculate the AV from the bead trajectories via (71).

$$\sigma^2_{AV}(\tau) = \frac{1}{2m^2(M - 2m + 1)} \sum_{j=1}^{M-2m+1} \left[\sum_{i=j}^{j+m-1} (\overline{x}_{i+m} - \overline{x}_i) \right]^2, \tag{9}$$

with $\overline{x}_i$ the position average of i^{th} bin. The position averages $\overline{x}_i$ of the positions x_n are given by

$$\overline{x}_i = \frac{1}{m} \sum_{n=i}^{i+m-1} x_n, \tag{10}$$

with $m = \tau/\tau_s$ (τ_s: sampling time) the overlapping bin lengths of the observation time intervals. The bin lengths define the number of bins $M = N - m + 1$ with N the total number of data points. Note that this corresponds to the so-called overlapping AV due to the consideration of overlapping time intervals. The closed-form expression of the AV for Eq. 6 is then given by (49)

$$\sigma^2_{AV}(\tau) = \frac{2k_BT\gamma}{\kappa^2\tau}\left(1 - \frac{3\gamma}{2\kappa\tau} + \frac{2\gamma}{\kappa\tau}e^{-\frac{\kappa\tau}{\gamma}} - \frac{\gamma}{2\kappa\tau}e^{-\frac{2\kappa\tau}{\gamma}}\right). \tag{11}$$

Hence, to use the AV to obtain κ, we calculate the AV of the measured x trajectory of the bead. Then, we follow a strategy reported by Morgan et al. (70) to fit the calculated AV to Eq. 11, with κ and γ being fitting parameters using maximum likelihood estimation (MLE).

Hadamard variance

In contrast to the AV, the HV is based on the calculation of the second position differences (second-order finite-difference method), which eliminates any additive linear signal contribution and thus renders it inherently insusceptible to linear drift. The overlapping HV is defined as (72).

$$\sigma^2_{HV}(\tau) = \frac{1}{6m^2(M - 3m + 1)} \sum_{j=1}^{M-3m+1} \left[\sum_{i=j}^{j+m-1} (\overline{x}_{i+2m} - 2\overline{x}_{i+m} + \overline{x}_i) \right]^2, \tag{12}$$

with $\overline{x}_i$ the position averages (Eq. 10; Fig. 3 *D*). The number of bins of the overlapping HV is given as $M = N - m + 1$. The closed-form expression of the HV of the bead motion (Eq. 6) then follows as

$$\sigma^2_{HV}(\tau) = \frac{2k_BT\gamma}{\kappa^2\tau}\left(1 - \frac{5\gamma}{3\kappa\tau} + \frac{5\gamma}{2\kappa\tau}e^{-\frac{\kappa\tau}{\gamma}} - \frac{\gamma}{\kappa\tau}e^{-\frac{2\kappa\tau}{\gamma}} + \frac{\gamma}{6\kappa\tau}e^{-\frac{3\kappa\tau}{\gamma}}\right). \tag{13}$$

The full derivation of the expression in Eq. 13 is given in the supporting material (section S3). To implement a computational method to calculate the HV from the bead trajectories and determine the trap stiffness κ and drag coefficient γ from the HV curves, we followed a similar strategy as Morgan et al. (70) employing an MLE fit of the HV as a function of observation times, with κ and γ being fitting parameters (Fig. 3 *E*). We implemented the HV method in a python framework that extends the Tweezepy package (70), which can be downloaded from https://github.com/alptug/tweezepy.

Note that, in principle, it is possible to include spectral correction factors for white, pink, and Brownian noise in Eqs. 8, 11, and 13, allowing one to correct for such types of noise when they are well understood and quantified. However, as the purpose of this study is the quantification of each methods' susceptibility to these types of additive noises, we do not include these corrections here.

We further quantify the uncertainties of the estimated parameters and bias in the force estimates of all three methods (supporting material, section S4, Figs. S4 and S5). We find that the uncertainties of the PSD, AV, and HV methods are approximately equal in the presence of colored noises and nonlinear drift, and all methods exhibit nonvanishing skewness in the distribution of relative errors, introducing bias. Therefore, in cases where

HV produces better estimates, it is due to a lower bias compared with the other methods.

MT experiments

MT setup

We use a custom-build MT setup equipped with two linear stepper motors (Physik Instrumente, Karlsruhe, Germany) to control the height of an external magnet (1 mm gap) above the flow cell and its rotation, and a Pifoc motor (Physik Instrumente, Karlsruhe, Germany) to adjust the focus of the objective (40× oil immersion, Olympus, Tokio, Japan) (17,37,73,74). Imaging of the diffraction rings of the magnetic beads uses a tube lens ($f = 150$ mm), a 650 nm LED (Thorlabs, Bergkirchen, Germany) for illumination, and an Optronis camera (CP80-25-M-72, Optronis, Kehl, Germany) operated at sampling frequencies of 72 Hz (full field of view) or 400 Hz (reduced field of view). Bead tracking is achieved with an open source Labview code that is based on a CUDA parallel computing algorithm and quadrant interpolation (24,45).

DNA and flow cell preparation

We use a 21 kbp long dsDNA construct derived from lambda phage DNA, which was prepared as described previously (75). The ends (∼ 600 bp) are functionalized for attachment with multiple digoxygenin (Roche, Woerden, The Netherlands) and biotin (Sigma-Aldrich, Burlington, MA, USA) molecules, respectively. Flow cells are built from two glass coverslips. The bottom slide (24×60 mm^2 (#1), VWR, Darmstadt, Germany) is first functionalized using (3-glycidoxypropyl)-trimethoxysilane (Thermo Fisher Scientific, Waltham, MA, USA), then incubated with polystyrene beads (Polysciences, Warrington, PA, USA) of 1 or 3 μm diameter in ethanol (VWR, Darmstadt, Germany), which serve as reference beads for drift correction. The top slide (24×60 mm^2 (#1.5), Carl Roth, Karlsruhe, Germany) contains two holes with diameters of ∼ 1 mm to connect the pump system (Ismatec, Germany) for fluid exchange in the flow chamber. Both slides sandwich a single layer of melted parafilm (Carl Roth, Karlsruhe, Germany) with a cutout to form a ∼ 50 μL channel that connects the inlet and outlet of the flow chamber. After assembly, the flow cell is incubated with 200 μg/mL anti-digoxygenin (Abcam, Cambridge, UK) in 1× PBS buffer (Sigma-Aldrich, Burlington, MA, USA) for at least 2 h to allow later DNA attachment via digoxygenin-anti-digoxygenin binding. The channel is rinsed with 1× PBS and passivated with 100 mg/mL BSA (Carl Roth, Karlsruhe, Germany) for 1 h to avoid nonspecific interactions, then rinsed again. We use commercial streptavidin-coated magnetic beads with diameters of 1 μm (DynaBeads MyOne Streptavidin C1, Thermo Fisher Scientific, Waltham, MA, USA) and 2.8 μm (DynaBeads M-270 Streptavidin, Thermo Fisher Scientific, Waltham, MA, USA) that are attached to the DNA via streptavidin-biotin binding. After coupling 1 μL of picomolar DNA stock with 2 μL MyOne beads or 13 μL M270 beads in 100 μL 1× PBS for around 30 s, we add the mixture to the flow cell and incubate for several minutes before flushing out unbound material with 1× PBS. The flow cell is mounted in a custom-built flow cell holder.

Force-calibration measurements

For the force-calibration measurements, we calibrate the distance between the magnet and upper cover slide of the flow cell by slowly approaching the top surface (to within 0.01 mm). We define the magnet position origin as the point where it touches the top coverslip. Next, the tethered magnetic beads are screened for attachment via multiple DNA molecules by measuring their response to force and torque. First, we apply negative turns (− 70 turns) at intermediate forces (2 or 14 pN for MyOne or M270 beads, respectively), where no change in extension is expected for beads tethered by single dsDNA molecules. Beads attached via multiple tethers form braids during negative rotation and thus decrease the extension. Multiple tethered beads are excluded from the measurements. Furthermore, the tethers are screened for single-strand breaks by overwinding the DNA at low force. We apply positive turns (70 turns) at low forces (0.05 or 0.14 pN for MyOne or M270 beads, respectively) and record the tether extension. Nicked tethers are not able to form plectonemes when overwound under low force and thus no change in extension is expected. For the force-calibration measurement, we record time traces of the bead-tether complex at 49 different magnet positions. We further record test traces at a low and high force, i.e., a fully relaxed and an unconstrained stretched DNA tether, to set the tether-bead coordinate system. In addition, we identify off-center attached beads, which do not follow a 2D Gaussian position distribution in the xy plane using the Shapiro-Wilk test for normality (exclusion criterion: $p < 0.05$) and exclude them from the experiment.

RESULTS AND DISCUSSION

We present and critically test different methods to analyze MT extension time traces for force calibration. To quantify and compare the accuracy of the PSD, AV, and HV methods in the presence of downsampling, colored noise, and drift, we first analyze simulated bead trajectories created by our Brownian dynamics simulations.

Testing the PSD, AV, and HV analyses using simulated bead trajectories

As a first step, we simulate ideal (noise-free) thermal motion trajectories (Fig. 2 *B* and materials and methods). We choose simulation time steps that are two orders of magnitude smaller than the characteristic (corner) time and within the stability region of the Milstein method (76). The corner frequency represents the turning point between purely diffusive bead motion and being constrained by the trap. To mimic the finite exposure time of the camera, we then downsample the trajectories by partitioning them into nonoverlapping windows whose widths match the exposure time of the camera and taking the average of each window. Next, we add either white, pink, or Brownian noise, or linear or nonlinear drift to the ideal thermal motion trace, since these are the most-common noise contributions to experimental MT data (supporting material, section S5). To test the effects of different levels of additive noise, we apply noise with different SNRs. The SNRs ($\mathrm{SNR_{dB}}$ in dB) are calculated as the ratio of the power of the ideal thermal motion trace (P_{sig}) to the powers of the pure additive noise (AN) traces P_{AN}, i.e., $\mathrm{SNR}_{dB} = 10\, log_{10}(P_{sig}/P_{AN})$. For linear drift, we add a linear trend of defined drift speed, or slope, to the ideal thermal motion trace.

To compare the three methods, i.e., PSD, AV, and HV, regarding their accuracy and precision in handling the different trajectory distortions, we next compute the PSD, AV, and HV for our simulated traces and fit the corresponding models, Eqs. 8, 11, and 13, respectively. We start by looking at 1 μm beads and two forces, 0.5 and 12 pN, and calculate the relative force errors according to $|1 - (F_{\mathrm{method}}/F_{\mathrm{true}})|$ with methods comprising PSD, AV, or HV (Fig. 4). In the presence of downsampling, all three methods (PSD, AV, and HV) reach a relative error of $\sim 7 \times 10^{-2}$ and $\sim 2 \times 10^{-2}$ for 0.5 and 12.0 pN,

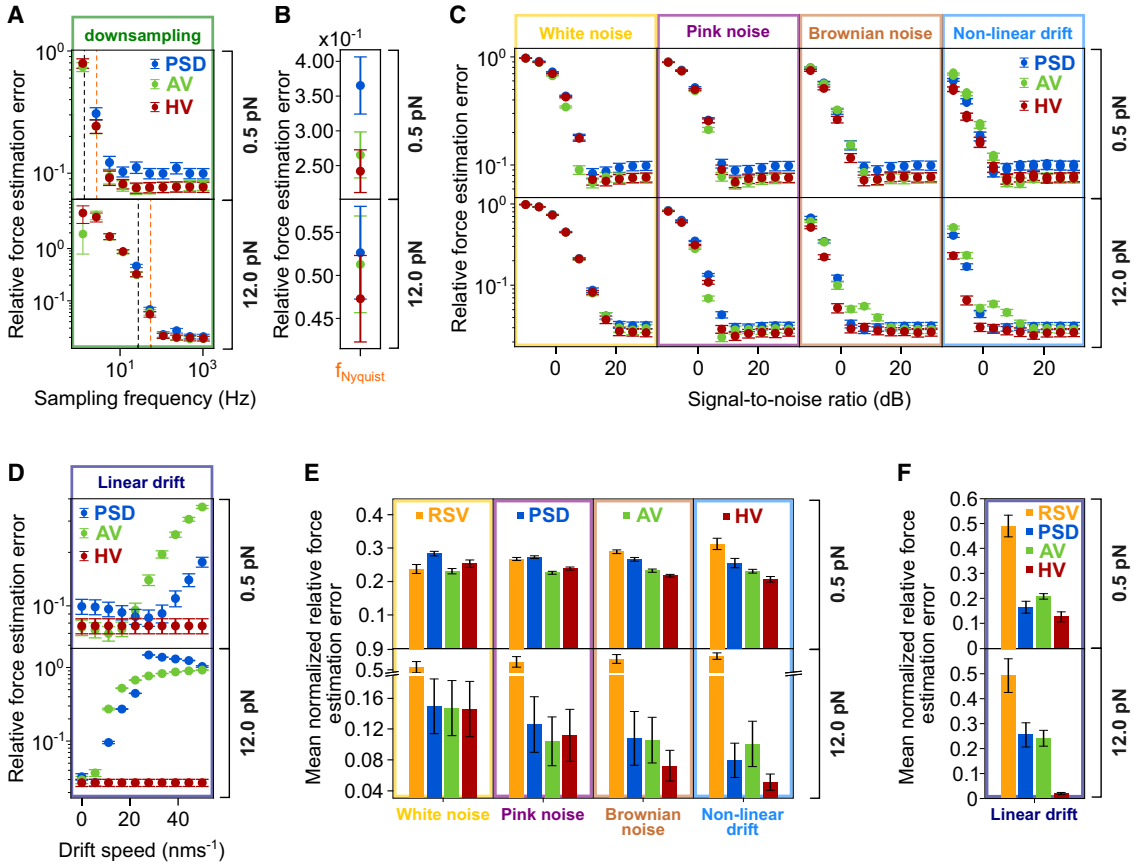

FIGURE 4 Effects of downsampling, colored noise, and drift on force estimation errors evaluated using simulated data. (*A*) Relative force estimation errors as a function of the sampling frequency for PSD (*blue*), AV (*green*), and HV (*red*) at low (0.5 pN) and high (12 pN) force. The black dashed lines highlight the corner frequencies and the orange dashed lines the Nyquist frequencies. Note: the PSD method failed to convergence at frequencies smaller than the corner frequencies. (*B*) Relative force estimation errors at the Nyquist frequency for PSD (*blue*), AV (*green*), and HV (*red*) at low (0.5 pN) and high (12 pN) force. (*C*) Relative force estimation errors as a function of the signal-to-noise ratios for PSD (*blue*), AV (*green*), and HV (*red*) at low (0.5 pN) and high (12 pN) force (sampling frequency: 72 Hz). (*D*) Relative force estimation errors as a function of the drift speed for PSD (*blue*), AV (*green*), and HV (*red*) at low (0.5 pN) and high (12 pN) force (sampling frequency: 72 Hz). (*E*) Mean (SNR) normalized relative force estimation errors of the real-space variance (RSV) (*orange*), PSD (*blue*), AV (green), and AV (*red*) at low (0.5 pN) and high (12 pN) force. The error bars represent the standard error of the mean. (*F*) Mean (drift speed) normalized relative force estimation errors of the RSV (*orange*), PSD (*blue*), AV (*green*), and AV (*red*) at low (0.5 pN) and high (12 pN) force. The error bars represent the standard error of the mean.

respectively, at sampling frequencies that exceed twice the corner frequency, i.e., the Nyquist frequency (Fig. 4 *A* and supporting material, section S6; Fig. S7). A stable plateau of low relative force errors is thus reached at sampling frequencies that fulfill the Nyquist theorem, i.e., exceed twice the characteristic frequency of the fluctuations. We calculate Nyquist frequencies of 2.75 and 54.81 Hz for 0.5 and 12 pN, respectively. At frequencies around and smaller than the Nyquist frequency, the relative force errors become on the same order as the applied force, indicating that the methods are not invariant to downsampling, as expected from the Nyquist theorem. However, taking a closer look at the critical regime of sampling at the Nyquist frequency ($f_s = f_{\mathrm{Nyquist}}$), the HV method results in slightly lower force estimation errors compared with the PSD and AV methods for 0.5 and 12.0 pN (Fig. 4 *B*). Considering the error bars, which correspond to one standard error, the differences between the methods are, however, statistically insignificant. Moreover, the PSD, AV, and HV methods achieve similar correction efficiencies, and all three methods perform significantly better than the RSV method (supporting material, section S7).

For the traces containing colored noise, we find that the relative errors for PSD, AV, and HV decrease with increasing SNRs in the presence of white, pink, and Brownian noise (Fig. 4 *C* and supporting material, section S8; Figs. S9–S12), until the relative errors essentially plateau for high SNRs. We find that the HV is on average most accurate in handling Brownian noise and nonlinear drift at low SNRs ≤ 10 dB (supporting material, section S9, Fig. S13). For white and pink noise, no clear trend between the different methods can be identified. For trajectories containing nonlinear drift, the HV clearly gives smaller force estimation errors over the whole SNR range compared with the PSD and AV methods.

Importantly, in the presence of linear drift, the relative force estimation errors increase with drift speed for the PSD and AV methods but stay constant for the HV method, which highlights its robustness against linear drift (Fig. 4 *D* and supporting material, section S10; Fig. S14).

In addition, we also simulate traces of the 1 μm beads at an intermediate force of 2.5 pN and of the 3 μm beads (representing M270) over a force range of 0.5–80 pN and observe similar trends (supporting material, sections S9 and S10).

To further give a more general overview of the force estimation accuracies of all methods, we next calculate the mean normalized relative force errors $\overline{\sigma}_{\mathrm{rel},i}$ by normalizing the relative force estimation errors σ_{rel} with respect to the methods (i,j) and summing over all SNRs or drift speeds using $\overline{\sigma}_{\mathrm{rel},i} = \sum_{\mathrm{SNR}\left(\text{or } v_{\mathrm{drift}}\right)} \left(\sigma_{\mathrm{rel},i}/\sum_j \sigma_{\mathrm{rel},j}\right)$ (Fig. 4, *D* and *E*). For comparison, here we also include the RSV method described in the introduction (Eq. 1). Note that a full analysis of the RSV in the presence of downsampling and additive noises is included in the supporting material, section S11.

As illustrated in Fig. 4 *D*, all four methods, i.e., RSV, PSD, AV, and HV, achieve almost equal accuracy with similar mean normalized force estimation errors at low force (0.5 pN) and in the presence of white and pink noise. However, the good apparent performance of the RSV is misleading and unreliable. As shown in the supporting material (section S11, Figs. S15–S26), the RSV exhibits significantly high relative force estimation errors at low and high SNRs and reaches a minimum error in the vicinity of 0 dB, where the variance contribution of downsampling and colored noises or drift cancel each other. This renders the RSV method unreliable as a force-calibration method. For Brownian noise, linear, and nonlinear drift, the HV method results in the smallest mean normalized force estimation errors compared with the PSD and AV (Fig. 4, *D* and *E*). At high force (12 pN), the PSD, AV, and HV methods perform much better than the RSV method, which is explained by the dominant effects of downsampling on the accuracy of the RSV method, for which the PSD, AV, and HV are approximately invariant at sampling frequencies larger than the Nyquist frequency. Note that, out of the three methods, the HV clearly performs best in the presence of Brownian noise, linear, and nonlinear drift, while performing similarly to PSD and AV for white and pink noise.

Together, our simulations show that the HV method is indeed the most stable, accurate, and precise in the presence of drift and performs very well for the other colored noise types, too. In addition, the relative errors using the PSD, AV, and HV methods to determine the variances of the motion trajectories decrease in the presence of white, pink, and Brownian noise with increasing SNRs, which is expected for decreasing noise levels. To further confirm the suitability of the HV as an accurate and drift-invariant method for force calibration in MT experiments, we apply the three methods to experimental data traces.

Application of PSD, AV, and HV to experimental data traces

Measurements are carried out using a 21 kbp dsDNA construct and MyOne (diameter $\approx$1 μm) beads. As sampling frequencies, we choose a rate that fulfills the Nyquist theorem to minimize downsampling effects, i.e., 72 Hz. The position of the external magnet is gradually changed over a wide translation range. At each magnet position the bead motion is tracked for several tens of seconds (Fig. 5 *A*). Simultaneously, reference beads are tracked and used to correct for global mechanical drift. We calculate the forces from the tracked and reference-corrected bead positions for each magnet height using all three methods, PSD, AV, and HV (Fig. 5, *B* and *C*). A typical force-calibration curve is shown in Fig. 5 *D*. The force decreases approximately exponentially with increasing magnet height, similar to the magnetic field (37). Furthermore, the extension of the DNA tether is well described by the 7-parameter WLC model (Fig. 5 *E*). From the WLC fit, we find a contour (L_c) and persistence (L_p) lengths of 6.8 μm and 44 nm, respectively, which are in good agreement with the expected crystallographic length of an $\sim$ 21 kbp DNA construct and with the literature values (37,62,75) for $L_p = 43 - 50$ nm.

Next, we determine the standard force estimation error from the covariance of the MLE fit to the experimental data (supporting material, section S12). Note that we do not know the ground truth of the forces that we calculate from experimental traces, making it difficult to confirm which method performs best in practice. However, one can examine how well each method is internally consistent, i.e., how well the MLE fits match the experimental data, which we use as a metric for confirming the accuracy of a method. Therefore, we calculate the relative force estimation errors (standard force estimation error over force) as a function of the force. We bin the relative errors to 12 force steps in total (Fig. 5 *F*). We find that over the whole force range, the HV method results in lower relative errors for the studied bead-tether system than the PSD and AV. On average, the HV errors are 18.0 and 9.4% lower compared with the PSD and AV, respectively. A similar trend is found for the M270 beads (diameter $\approx$2.8 μm; supporting material, section S13, Fig. S27). This finding indicates that the HV method is the most precise in analyzing the experimental data. In addition, we assess the stability of the HV method by adding artificial linear drift to the experimental data in the x and y directions and evaluating the resulting relative force estimation errors (supporting material, section S14, Fig. S28). As the drift speed increases, the relative force estimation errors for the PSD and AV methods increase, and their applied force estimates per magnet position reduce significantly. In contrast, the HV method

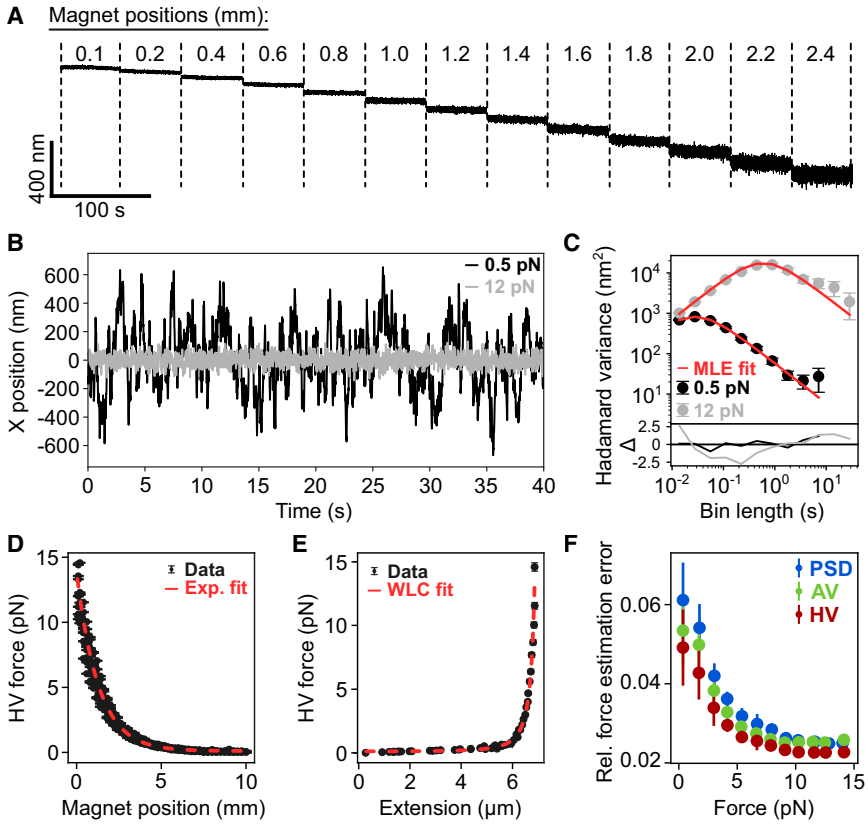

FIGURE 5 Force calibration using experimental MT data. (*A*) Experimental extension time traces (z dimension) at different magnet positions corresponding to different forces. (*B*) Experimental data traces (x dimension) at low (0.5 pN) and high (12 pN) force. (*C*) Hadamard variance of the experimental traces shown in (*B*) at low (0.5 pN) and high (12 pN) force. The red lines represent the MLE fits. (*D*) HV force versus magnet position plot of 13 beads. From the exponential fit (*red dashed line*), we find a maximum force of 13.9 pN. The error bars are $\sqrt{2}\sigma$. (*E*) HV force-extension plot of one bead. Error bars correspond to one standard deviation. The contour and persistence lengths derived from the WLC fit (*red dashed line*) are 6.8 μm and 44 nm, respectively. (*F*) Relative force estimation errors of experimental data for PSD (*blue*), AV (*green*), and HV (*red*). Data are derived from experimental force-calibration traces of 13 MyOne beads (diameter ≈ 1 μm, sampling frequency: 72 Hz). Error bars are one standard deviation.

is completely unaffected. As a control, we also analyze the relative bead-to-bead force errors and find a force uncertainty of $\sim 11\%$, which is in good agreement with previous articles (37,44) that report a bead-to-bead variability of approximately 10%, which is dominated by differences in bead volumes and magnetic particle content (supporting material, section S15, Fig. S29). Notably, this error is the same for all three methods demonstrating that the bead-to-bead variations are a systematic error of the system and independent of the applied method.

CONCLUSION

In conclusion, we introduce a robust thermal motion-based method using the HV for processing and analyzing multiplexed MT data with high accuracy. By addressing common sources of additive noise in comparison with conventional methods such as the RSV, the PSD, and the AV, we find that the HV method offers important improvements in force-calibration precision. Through extensive testing with Brownian dynamics simulations, replicating typical experimental MT conditions, and including controlled levels of common colored noise types and drift, we demonstrate the superior performance of the HV method across a wide range of SNRs and drift speeds. Notably, our results show consistently lower force estimation errors with the HV method, particularly in the presence of Brownian noise and nonlinear drift at SNR ≤ 10 dB, and excellent stability in the presence of linear drift, ensuring reliable results across varying experimental conditions. Application of the HV method to experimental data sets further validates its effectiveness, revealing an average reduction of force estimation errors by 18.0 and 9.4% compared with the PSD and AV methods, respectively. These findings highlight the suitability of the HV method for accurate force calibration, which is important for achieving sub-pN resolution and precision in multiplexed MT experiments.

Although the HV method has fewer degrees of freedom for the distribution of a single stability estimate compared with the AV method, the lost information primarily reflects pathological effects such as linear drift. The HV method outperforms the AV and PSD methods at higher forces (≥ 12 pN), while the AV method shows marginal improvements at lower forces (~ 0.5 pN) in the presence of white and pink noise. Given that experimental data tend to include additional colored noise and drift, beyond white and pink noise, the HV method overall is the more reliable option. The HV approach consistently delivers equal or more accurate and precise force calibrations in MT devices, outperforming both the AV and PSD methods in practice. In terms of computational demands, the HV and AV methods are comparable and less demanding than the PSD method.

In summary, our study contributes a new force-calibration method to the existing repertoire, offering researchers a powerful tool for obtaining accurate results that are essential for advancing our understanding of molecular-scale interactions and mechanical processes in biological systems. For this purpose, we make our approach widely accessible via a clearly documented open-source implementation of the HV method as an extension of the existing Tweezepy (70) package.

ACKNOWLEDGMENTS

This work was supported by the European Research Council through the Consolidator Grant "ProForce" and the Dutch Research Council (NWO) with grant no. OCENW.GROOT.2019.071. S.D.P. was further supported by the Alexander-von-Humboldt foundation through a Feodor-Lynen fellowship. The authors thank Dave van den Heuvel and Elleke van Harten for laboratory assistance.

AUTHOR CONTRIBUTIONS

S.D.P. and A.U. contributed equally to this work by designing and performing the research, contributing analytic tools, analyzing data, and writing the paper. C.K. contributed to the research and coauthored the paper. L.F. and J.L. cosupervised the project, coauthored the paper, and acquired funding for the project.

DECLARATION OF INTERESTS

The authors declare no competing interests.

SUPPORTING CITATIONS

The following are cited in the supporting material: (77–83).

SUPPORTING MATERIAL

Supporting material can be found online at https://doi.org/10.1016/j.bpj.2024.10.008.

REFERENCES

1. De Vlaminck, I., and C. Dekker. 2012. Recent advances in magnetic tweezers. *Annu. Rev. Biophys.* 41:453–472.
2. Bustamante, C., Z. Bryant, and S. B. Smith. 2003. Ten years of tension: single-molecule DNA mechanics. *Nature.* 421:423–427.
3. Neuman, K. C., and A. Nagy. 2008. Single-molecule force spectroscopy: optical tweezers, magnetic tweezers and atomic force microscopy. *Nat. Methods.* 5:491–505.
4. Lipfert, J., M. M. van Oene, …, N. H. Dekker. 2015. Torque Spectroscopy for the Study of Rotary Motion in Biological Systems. *Chem. Rev.* 115:1449–1474.
5. Krieg, M., G. Fläschner, …, D. J. Müller. 2019. Atomic force microscopy-based mechanobiology. *Nat. Rev. Phys.* 1:41–57.
6. Kriegel, F., W. Vanderlinden, …, J. Lipfert. 2018. Nanoscale Imaging. *In* Section Measuring Single-Molecule Twist and Torque in Multiplexed Magnetic Tweezers. Springer Nature, New York, NY, pp. 75–98.
7. Strick, T. R., V. Croquette, and D. Bensimon. 2000. Single-molecule analysis of DNA uncoiling by a type II topoisomerase. *Nature.* 404:901–904.
8. Abbondanzieri, E. A., W. J. Greenleaf, …, S. M. Block. 2005. Direct observation of base-pair stepping by RNA polymerase. *Nature.* 438:460–465.
9. Herbert, K. M., W. J. Greenleaf, and S. M. Block. 2008. Single-Molecule Studies of RNA Polymerase: Motoring Along. *Annu. Rev. Biochem.* 77:149–176.
10. Finer, J. T., R. M. Simmons, and J. A. Spudich. 1994. Single myosin molecule mechanics: piconewton forces and nanometre steps. *Nature.* 368:113–119.
11. Thomas, W. E., V. Vogel, and E. Sokurenko. 2008. Biophysics of Catch Bonds. *Annu. Rev. Biophys.* 37:399–416.
12. Dulin, D., J. Lipfert, …, N. H. Dekker. 2013. Studying genomic processes at the single-molecule level: introducing the tools and applications. *Nat. Rev. Genet.* 14:9–22.
13. Almaqwashi, A. A., T. Paramanathan, …, M. C. Williams. 2016. Mechanisms of small molecule–DNA interactions probed by single-molecule force spectroscopy. *Nucleic Acids Res.* 44:3971–3988.
14. Ritzefeld, M., V. Walhorn, …, N. Sewald. 2013. Analysis of DNA interactions using single-molecule force spectroscopy. *Amino Acids.* 44:1457–1475.
15. Ott, W., M. A. Jobst, …, M. A. Nash. 2017. Single-molecule force spectroscopy on polyproteins and receptor–ligand complexes: The current toolbox. *J. Struct. Biol.* 197:3–12.
16. Zhuang, X., and M. Rief. 2003. Single-molecule folding. *Curr. Opin. Struct. Biol.* 13:88–97.
17. Bauer, M. S., S. Gruber, …, J. Lipfert. 2022. A tethered ligand assay to probe SARS-CoV-2:ACE2 interactions. *Proc. Natl. Acad. Sci. USA.* 119:e2114397119.
18. Alegre-Cebollada, J. 2021. Protein nanomechanics in biological context. *Biophys. Rev.* 13:435–454.
19. Neuman, K. C., S. M. Block, and S. M. Block. 2004. Optical trapping. *Rev. Sci. Instrum.* 75:2787–2809.
20. Gieseler, J., J. R. Gomez-Solano, …, G. Volpe. 2021. Optical tweezers — from calibration to applications: a tutorial. *Adv. Opt. Photonics.* 13:74–241.
21. Volpe, G., O. M. Maragò, …, G. A. Swartzlander. 2023. Roadmap for optical tweezers. *J. Phys. Photonics.* 5:022501.
22. Löf, A., U. Walker Philipp, …, J. Lipfert. 2019. Multiplexed protein force spectroscopy reveals equilibrium protein folding dynamics and the low-force response of von Willebrand factor. *Proc. Natl. Acad. Sci. USA.* 116:18798–18807.
23. Agarwal, R., and K. E. Duderstadt. 2020. Multiplex flow magnetic tweezers reveal rare enzymatic events with single molecule precision. *Nat. Commun.* 11:4714.
24. Cnossen, J. P., D. Dulin, and N. H. Dekker. 2014. An optimized software framework for real-time, high-throughput tracking of spherical beads. *Rev. Sci. Instrum.* 85:103712.
25. Ribeck, N., and O. A. Saleh. 2008. Multiplexed single-molecule measurements with magnetic tweezers. *Rev. Sci. Instrum.* 79:094301.
26. Kruithof, M., F. Chien, …, J. van Noort. 2008. Subpiconewton Dynamic Force Spectroscopy Using Magnetic Tweezers. *Biophys. J.* 94:2343–2348.
27. Bausch, A. R., W. Möller, and E. Sackmann. 1999. Measurement of local viscoelasticity and forces in living cells by magnetic tweezers. *Biophys. J.* 76:573–579.
28. Popa, I., J. A. Rivas-Pardo, …, J. M. Fernández. 2016. A HaloTag Anchored Ruler for Week-Long Studies of Protein Dynamics. *J. Am. Chem. Soc.* 138:10546–10553.
29. Lipfert, J., M. Lee, …, N. H. Dekker. 2014. Magnetic Tweezers for the Measurement of Twist and Torque. *JoVE.* 87:e51503.

30. Lipfert, J., J. W. J. Kerssemakers, …, N. H. Dekker. 2010. Magnetic torque tweezers: measuring torsional stiffness in DNA and RecA-DNA filaments. *Nat. Methods.* 7:977–980.
31. Lipfert, J., M. Wiggin, …, N. H. Dekker. 2011. Freely orbiting magnetic tweezers to directly monitor changes in the twist of nucleic acids. *Nat. Commun.* 2:439.
32. Florin, E. L., A. Pralle, …, J. K. H. Hörber. 1998. Photonic force microscope calibration by thermal noise analysis. *Appl. Phys. A.* 66:S75–S78.
33. Strick, T. R., J.-F. Allemand, …, V. Croquette. 1996. The Elasticity of a Single Supercoiled DNA Molecule. *Science.* 271:1835–1837.
34. Vilfan, I. D., J. Lipfert, …, N. Dekker. 2009. Handbook of Single-Molecule Biophysics. *In* Magnetic tweezers for single-molecule experiments. Springer, New York, NY, pp. 371–395.
35. Felgner, H., O. Müller, and M. Schliwa. 1995. Calibration of light forces in optical tweezers. *Appl. Opt.* 34:977–982.
36. Bausch, A. R., F. Ziemann, …, E. Sackmann. 1998. Local measurements of viscoelastic parameters of adherent cell surfaces by magnetic bead microrheometry. *Biophys. J.* 75:2038–2049.
37. Lipfert, J., X. Hao, and N. H. Dekker. 2009. Quantitative Modeling and Optimization of Magnetic Tweezers. *Biophys. J.* 96:5040–5049.
38. Marko, J. F., and E. D. Siggia. 1995. Stretching dna. *Macromolecules (Washington, DC, U. S.).* 28:8759–8770.
39. Bustamante, C., J. F. Marko, …, S. Smith. 1994. Entropic Elasticity of λ-Phage DNA. *Science.* 265:1599–1600.
40. Bouchiat, C., M. D. Wang, …, V. Croquette. 1999. Estimating the persistence length of a worm-like chain molecule from force-extension measurements. *Biophys. J.* 76:409–413.
41. Smith, S. B., Y. Cui, and C. Bustamante. 1996. Overstretching B-DNA: The Elastic Response of Individual Double-Stranded and Single-Stranded DNA Molecules. *Science.* 271:795–799.
42. te Velthuis, A. J. W., J. W. J. Kerssemakers, …, N. H. Dekker. 2010. Quantitative Guidelines for Force Calibration through Spectral Analysis of Magnetic Tweezers Data. *Biophys. J.* 99:1292–1302.
43. Yu, Z., D. Dulin, …, N. H. Dekker. 2014. A force calibration standard for magnetic tweezers. *Rev. Sci. Instrum.* 85:123114.
44. Ostrofet, E., F. S. Papini, and D. Dulin. 2018. Correction-free force calibration for magnetic tweezers experiments. *Sci. Rep.* 8:15920.
45. van Loenhout, M. T. J., J. W. J. Kerssemakers, …, C. Dekker. 2012. Non-Bias-Limited Tracking of Spherical Particles, Enabling Nanometer Resolution at Low Magnification. *Biophys. J.* 102:2362–2371.
46. Dulin, D., T. J. Cui, …, N. H. Dekker. 2015. High spatiotemporal-resolution magnetic tweezers: calibration and applications for DNA dynamics. *Biophys. J.* 109:2113–2125.
47. Huhle, A., D. Klaue, …, R. Seidel. 2015. Camera-based three-dimensional real-time particle tracking at kHz rates and Ångström accuracy. *Nat. Commun.* 6:5885.
48. Wong, W. P., and K. Halvorsen. 2006. The effect of integration time on fluctuation measurements: calibrating an optical trap in the presence of motion blur. *Opt Express.* 14:12517–12531.
49. Lansdorp, B. M., and O. A. Saleh. 2012. Power spectrum and Allan variance methods for calibrating single-molecule video-tracking instruments. *Rev. Sci. Instrum.* 83:025115.
50. Shon, M. J., S.-H. Rah, and T.-Y. Yoon. 2019. Submicrometer elasticity of double-stranded DNA revealed by precision force-extension measurements with magnetic tweezers. *Sci. Adv.* 5:eaav1697.
51. Lukić, B., S. Jeney, …, E. L. Florin. 2005. Direct Observation of Nondiffusive Motion of a Brownian Particle. *Phys. Rev. Lett.* 95:160601.
52. Ostrofet, E., F. S. Papini, and D. Dulin. 2020. High spatiotemporal resolution data from a custom magnetic tweezers instrument. *Data Brief.* 30:105397.
53. Nørrelykke, S. F., and H. Flyvbjerg. 2010. Power spectrum analysis with least-squares fitting: Amplitude bias and its elimination, with application to optical tweezers and atomic force microscope cantilevers. *Rev. Sci. Instrum.* 81:075103.
54. Vasilescu, G. 2005. Electronic Noise and Interfering Signals: Principles and Applications. Springer Science & Business Media, Berlin, Heidelberg, Germany.
55. Gillespie, D. T. 1996. The mathematics of Brownian motion and Johnson noise. *Am. J. Phys.* 64:225–240.
56. Szendro, P., G. Vincze, and A. Szasz. 2001. Pink-noise behaviour of biosystems. *Eur. Biophys. J.* 30:227–231.
57. Walter, J. C., A. Ferrantini, …, C. Vanderzande. 2012. Fractional Brownian motion and the critical dynamics of zipping polymers. *Phys. Rev. E.* 85:031120.
58. Li, T., and M. G. Raizen. 2013. Brownian motion at short time scales. *Ann. Phys.* 525:281–295.
59. Pratt, W. K., J. Kane, and H. C. Andrews. 1969. Hadamard transform image coding. *Proc. IEEE.* 57:58–68.
60. Baugh, R. A. 1971. Frequency modulation analysis with the Hadamard variance. *In* 25th Annual Symposium on Frequency Control IEEE, pp. 222–225.
61. Wan, K.-W., E. Vilar, and J. Roberts. 1989. Extended Variances and Autoregressive/Moving Average Algorithm for the Measurement and Synthesis of Oscillator Phase Noise. *In* Proceedings of the 43rd Annual Symposium on Frequency Control IEEE, pp. 331–335.
62. Burnham, D. R., I. De Vlaminck, …, C. Dekker. 2014. Skewed brownian fluctuations in single-molecule magnetic tweezers. *PLoS One.* 9:e108271.
63. Faxén, H. 1922. Der Widerstand gegen die Bewegung einer starren Kugel in einer zähen Flüssigkeit, die zwischen zwei parallelen ebenen Wänden eingeschlossen ist. *Ann. Phys.* 373:89–119.
64. Leach, J., H. Mushfique, …, M. J. Padgett. 2009. Comparison of Faxén's correction for a microsphere translating or rotating near a surface. *Phys. Rev. E.* 79:026301.
65. Milstein, G. 1975. Approximate integration of stochastic differential equations. *Theor. Probab. Appl.* 19:557–562.
66. Timmer, J., and M. Koenig. 1995. On generating power law noise. *Astron. Astrophys.* 300:707.
67. Sellar, R. G., and G. D. Boreman. 2005. Comparison of relative signal-to-noise ratios of different classes of imaging spectrometer. *Appl. Opt.* 44:1614–1624.
68. Kim, K., and O. A. Saleh. 2009. A high-resolution magnetic tweezer for single-molecule measurements. *Nucleic Acids Res.* 37:e136.
69. Zhou, Y., Q. Tang, …, J. Yan. 2023. A novel design for magnetic tweezers with wide-range temperature control. *Biophys. J.* 122:3860–3868.
70. Morgan, I. L., and O. A. Saleh. 2021. Tweezepy: A Python package for calibrating forces in single-molecule video-tracking experiments. *PLoS One.* 16:e0262028.
71. Howe, D. A., D. Allan, and J. Barnes. 1981. Properties of signal sources and measurement methods. *In* Thirty Fifth Annual Frequency Control Symposium IEEE, pp. 669–716.
72. Riley, W. J. 2008. Handbook of Frequency Stability Analysis. National Institute of Standards and Technology.
73. Walker, P. U., W. Vanderlinden, and J. Lipfert. 2018. Dynamics and energy landscape of DNA plectoneme nucleation. *Phys. Rev. E.* 98:042412.
74. Kriegel, F., N. Ermann, …, J. Lipfert. 2017. Probing the salt dependence of the torsional stiffness of DNA by multiplexed magnetic torque tweezers. *Nucleic Acids Res.* 45:5920–5929.
75. Lipfert, J., D. A. Koster, …, N. H. Dekker. 2009. DNA Topoisomerases. *In* Section Single-Molecule Magnetic Tweezers Studies of Type IB Topoisomerases. Springer, New York, NY, pp. 71–89.
76. Buckwar, E., and T. Sickenberger. 2011. A comparative linear mean-square stability analysis of Maruyama-and Milstein-type methods. *Math. Comput. Simulat.* 81:1110–1127.
77. Ashby, N., and B. Patla. 2016. Simulations of the Hadamard Variance: Probability Distributions and Confidence Intervals. *IEEE Trans. Ultrason. Ferroelectrics Freq. Control.* 63:636–645.

78. Riley, W., and C. Greenhall. 2004. Power law noise identification using the lag 1 autocorrelation. *In* 2004 18th European Frequency and Time Forum (EFTF 2004) IET, pp. 576–580.

79. Holt, C. C. 2004. Forecasting seasonals and trends by exponentially weighted moving averages. *Int. J. Forecast.* 20:5–10.

80. Winters, P. R. 1960. Forecasting sales by exponentially weighted moving averages. *Manag. Sci.* 6:324–342.

81. Liu, F. T., K. M. Ting, and Z.-H. Zhou. 2008. Isolation forest. *In* 2008 Eighth Ieee International Conference on Data Mining IEEE, pp. 413–422.

82. Liu, F. T., K. M. Ting, and Z.-H. Zhou. 2012. Isolation-based anomaly detection. *ACM Trans. Knowl. Discov. Data.* 6:1–39.

83. Doob, J. L. 1942. The Brownian movement and stochastic equations. *Ann. Math.* 43:351–369.